1 Investigating the Intercalation Chemistry of Alkali Ions in Fluoride **2 Perovskites**

- 3 Tanghong Yi,^{†,‡} Wei Chen,^{‡,¶} Lei Cheng,^{‡,§} Ryan D. Bayliss,[†] Feng Lin,^{‡,∥} Michael R. Plews,[†]
 4 Dennis Nordlund,[⊥] Marca M. Doeff,[‡] Kristin A. Persson,[‡] and Jordi Cabana*,[†]
- 5 [†]Department of Chemistry, University of Illinois at Chicago, Chicago, Illinois 60607, United States
- 6 [‡]Energy Storage and Distributed Resources Division, Lawrence Berkeley National Laboratory, Berkeley, California 94720, United
- States

12

13

15

16

17

18

19

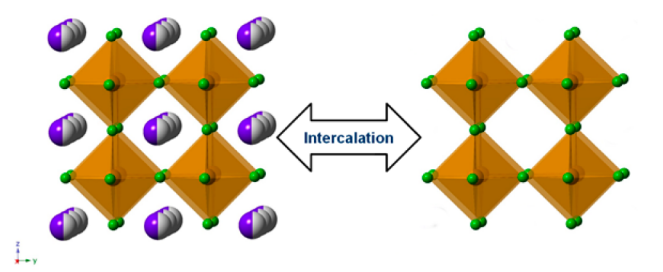
2.0

21

- §Department of Materials Science and Engineering, University of California Berkeley, Berkeley, California 94720, United States
- 9 LAC National Accelerator Laboratory, 2575 Sand Hill Road MS69, Menlo Park, California 94025, United States
- 10 ¶Department of Mechanical, Materials, and Aerospace Engineering, Illinois Institute of Technology, Chicago, Illinois 60616, United

Supporting Information

ABSTRACT: Reversible intercalation reactions provide the basis for modern battery electrodes. Despite decades of 14 exploration of electrode materials, the potential for materials in the nonoxide chemical space with regards to intercalation chemistry is vast and rather untested. Transition metal fluorides stand out as an obvious target. To this end, we report herein a new family of iron fluoride-based perovskite cathode materials $A_xK_{1-x}FeF_3$ (A = Li, Na). By starting with KFeF₃, approximately 75% of K⁺ ions were subsequently replaced by Li⁺ and Na⁺ through electrochemical means. X-ray diffraction and Fe X-ray



22 absorption spectroscopy confirmed the existence of intercalation of alkali metal ions in the perovskite structure, which is 23 associated with the $Fe^{2+/3+}$ redox couple. A computational study by density functional theory showed agreement with the 24 structural and electrochemical data obtained experimentally, which suggested the possibility of fluoride-based materials as 25 potential intercalation electrodes. This study increases our understanding of the intercalation chemistry of ternary fluorides, 26 which could inform efforts toward the exploration of new electrode materials.

■ INTRODUCTION

29 The study of the intercalation chemistry of alkali ions in 30 transition metal-containing hosts has fascinated scientists for 31 the past 40 years. The ability to intercalate large amounts of lithium enabled the advent of modern Li-ion batteries. It is also at the core of many efforts to develop next-generation energy 34 storage solutions to enable the integration of renewable energy 35 sources for a modern sustainable society. With major challenges 36 arising from the difficulties in achieving high energy density and 37 extended life at a reasonable cost, new battery chemistries for 38 electric vehicles and smart grids applications are a field of 39 intensive research. Searching for new electrode materials to 40 replace the oxide cathodes used currently in Li-ion technologies 41 is the fastest way toward leaps in storage capability. The 42 underlying reason is that current cathodes possess about half of 43 the reversible specific capacity of the commercial graphite 44 anodes and, as a result, are the limiting components.

The chemistry of fluoride-containing compounds has been of 46 historic interest due to the highly electronegative nature of the 47 ion. The highly ionic nature of the transition metal-fluoride 48 bonds elevates the redox potential of the material and renders 49 fluorides interesting in the search for an intercalation cathode

that enables devices with high energy density. It is also of 50 interest that these highly electronegative species might be able 51 to stabilize highly oxidized transition metals upon high rate 52 cycling, which would lead to better safety through the reduced 53 likelihood of material degradation. Among the redox-active 54 transition metals, iron is particularly attractive due to its 55 abundance, cost, and environmentally benign nature. Prior to 56 this report, a few binary iron fluoride phases (FeF3, FeF2, and 57 $\text{FeF}_3 \times \text{H}_2\text{O})^{2-7}$ and mixed-anion compounds $(\text{FeOF})^{8-10}$ have 58 been studied as active materials for electrochemical energy 59 storage. 2,5,11-15 However, most of these phases were found to 60 react through conversion mechanisms, where the fluoride 61 compounds are reduced all the way to metallic particles and 62 LiF. This mechanism results in severe capacity losses during 63 cycling. 16 To incorporate Li into the cathode, as required to 64 pair it with Li-free graphite anodes, a nanocomposite of FeF₂ 65 and LiF has been investigated.³ This nanocomposite also shows 66 a very complex transformation mechanism with the hypothe- 67

68 sized existence of intermediate ternary phases of poor 69 crystallinity. The outcome was still a deficient ability to cycle 70 reversibly.

Topotactic intercalation mechanisms, where atomic arrange-72 ments are not severely disrupted, continue to be preferred in 73 the design of new cathode materials. 17 Aside from the small 74 solubility of Li in FeF₃ (to roughly Li_{0.5}FeF₃) before 75 conversion, only Li₃FeF₆ and LiFe₂F₆ were clearly shown to 76 possess electrochemical activity through intercalation mecha-77 nisms. ^{18–20} Other iron based fluorides such as LiNiFeF₆²¹ and 78 Na₃FeF₆²² have been experimentally synthesized and studied, 79 but their electrochemical properties were rather poor. Most of 80 these ternary phases contain Fe (III), 23,24 which is difficult to 81 oxidize further during the initial lithium deintercalation (cell 82 charge). No reports were found of the electrochemical 83 properties of Li–Fe(II)–F phases, although some of the 84 ternaries, such as LiFeF₃ and Li₂FeF₄, 25 have been predicted to 85 exist by first-principles calculations. In contrast, ternary phase 86 Fe(II) fluorides with other alkali metals are known such as 87 K₂FeF₄, KFeF₃, and NaFeF₃. ²⁶⁻²⁸ KFeF₃ has a cubic perovskite 88 (ABX₃) structure (space group $Pm\overline{3}m$), where Fe ions sit at the 89 B-site, six-fold coordinated with F ions, and K ions reside in the 90 A-site, 12-fold coordinated with F ions. The idealized cubic 91 perovskite structure is expected to exist within certain values of 92 the tolerance factor, $t = (r_A + r_O)/\sqrt{2(r_B + r_O)}$, where r_A , r_B , 93 and r_0 are ionic radii for A, B, and O, respectively.²⁹ When t is 94 lower than 0.75, the perovskite structure will tend to deviate 95 from the cubic ideal form while attempting to reduce bonding 96 strain. ^{29,30} The tolerance factors for KFeF₃, NaFeF₃, and LiFeF₃ 97 (where $r_{\rm F}$ is substituted for $r_{\rm O}$ in the equation above) are 98 around 0.91, 0.79, and 0.70, respectively, assuming they all 99 retain the perovskite structure. In fact, NaFeF₃ has been shown 100 to distort to an orthorhombic symmetry structure. 28,31 101 Likewise, LiFeF3 would be expected to exist in a lower 102 symmetry system if it can be made.

Perovskites constitute a family of materials that exhibit many 104 interesting properties and are widely used in modern chemical 105 industry as catalysts, ²⁹ solid oxide fuel cell components, ^{32–35} solar cells³⁶ and phosphors,³⁷ among many other applications. Recently, there have been extensive studies on perovskites as solid electrolytes for Li-ion batteries due to their fast ionic 109 conduction and as electrocatalysts for Li-O_2 batteries and 110 regenerative fuel cells. However, very limited study on 111 perovskites as battery electrode materials has been reported, 112 despite the intrinsic high diffusion rate of ions in many 113 perovskite phases. Since LiFeF₃, if existent, is unlikely to 114 crystallize in the perovskite structure because of the small ionic 115 radius of Li⁺ (76 pm) with respect to the A cavity, we explored 116 perovskite structures with Fe²⁺ and mixed K/alkali metal (Li or 117 Na) contents, $A_xK_{1-x}FeF_3$ (A = Li, Na). This outcome was 118 achieved by electrochemically replacing the large alkali ion with 119 smaller Li or Na. Herein, we report the synthesis, electro-120 chemical behavior, and physical characterization of the 121 compounds. The resulting phases showed reversible intercala-122 tion chemistry leveraging the Fe²⁺/Fe³⁺ redox couple.

3 ■ EXPERIMENTAL METHODS

124 KFe F_3 was synthesized through conventional solid-state chemistry 125 method. In the solid-state method, KF (powder, Sigma-Aldrich, \geq 126 99.99%) and Fe F_2 (powder, Sigma-Aldrich) were used as starting 127 materials. They were mixed in stoichiometric ratios in a tungsten 128 carbide jar on a SPEX SamplePrep 8000 M mixer/mill for 30 min. The

mixture was pressed into pellets, placed in Pt crucibles, and annealed at 129500 °C for 12 h under Ar gas flow.

Electrochemical experiments were conducted in two-electrode 2032 131 coin-type cells. Lithium or sodium metal was used as both the counter 132 and pseudoreference electrode, and a solution of either 1 M LiPF₆ or 133 NaPF₆ dissolved in 1:1 volume mixture of ethylene carbonate (EC)/ 134 dimethyl carbonate (DMC) was used as the electrolytic solution. The 135 solution for Na cells was made in-house, while that for the lithium cells 136 was purchased from Novolyte. Cells were assembled in an argon-filled 137 glovebox. Electrochemical measurements were conducted using a 138 VMP3 potentiostat at room temperature. Galvanostatic cycling was 139 conducted at a current rate of C/30, where C was defined as 223 and 140 197 mA h/g for Li (LiFeF₃) and Na (NaFeF₃) cells, respectively 141 (theoretical capacities of LiFeF3 and NaFeF3, respectively). However, 142 the capacities of $A_rK_{1-r}FeF_3$ (A = Li, Na) compounds in this paper 143 were calculated based on the weight of KFeF3, which was the starting 144 material in the electrodes contained in the cells. Composite electrodes 145 were prepared by mixing KFeF3 and carbon black in a 6 wt % 146 polyvinylidene difluoride (PVDF) solution in 1-methyl-2-pyrrolinone 147 (NMP), to reach an active material/binder/carbon weight ratio of 148 45:45:10. KFeF₃ and carbon black were premixed in a planetary ball 149 mill (Retsch PM 100) at 500 rpm for 12 h. The slurry was mixed until 150 homogeneity was reached and was subsequently cast onto Al foil using 151 a doctor blade. All the electrode processing was done inside an argon 152 filled glovebox. The electrodes were left to dry under ambient 153 temperature in the glovebox overnight before being placed in a 154 vacuum oven at 110 °C for 12 h.

The composition and crystallinity of the KFeF $_3$ samples were 156 evaluated by powder X-ray diffraction (XRD). Patterns were collected 157 between 10° and 80°, 2 θ , at a rate of 0.02°/min using a Bruker D2 158 phaser diffractometer using Cu K α radiation (λ = 1.5418 Å). 159 Operando synchrotron XRD data were collected on beamline 11–3 160 at the Stanford Synchrotron Radiation Lightsource (SSRL, Menlo 161 Park, CA) with a Si (311) crystal monochromator. Data were collected 162 continuously in 3 min acquisitions on the coin cell in transmission 163 geometry during cycling. A special 2032 coin-type cell was made with a 164 hole in the center of the spacer, bottom, and top coin cell parts for the 165 beam path. The coin-type cell was subsequently sealed in a pouch 166 with two leads to connect the electrodes to the cycler. The stage was 167 rocked by 0.02 mm during beam exposure to minimize beam damage. 168 Both LaB $_6$ and the current collector Al were used as external and 169 internal standards, respectively.

The particle sizes and morphologies of samples were analyzed using 171 scanning electron microscopy (SEM). Micrographs were collected on 172 a JEOL 7500F microscope operated at 15 kV and 20 mA in SEM 173 mode, and the elemental distribution of samples was examined with an 174 energy dispersive X-ray spectroscopy (EDS) detector (Thermo- 175 Fisher). The electrodes for EDS were recovered from cycled coin 176 cells and washed with DMC in an argon-filled glovebox.

Soft X-ray absorption spectroscopy (XAS) measurements were 178 carried out on the 33-pole wiggler beamline 10-1 at the Stanford 179 Synchrotron Radiation Lightsource (SSRL, Menlo Park, CA) using a 180 ring current of 350 mA and a $1000 \times 1~\text{mm}^{-1}$ spherical grating 181 monochromator with 20 μ m entrance and exit slits. Data were 182 obtained at a spectral resolution of $\sim 0.2~\text{eV}$ in fluorescence yield (FY) 183 mode to acquire bulk information on the material. The angle of 184 incidence in FY mode was selected so as to minimize self-absorption 185 while still being bulk sensitive. The beam footprint on the sample was 186 1 mm². Samples were attached to a bar-shape aluminum sample holder 187 using conductive carbon tape. All samples for soft XAS study were 188 KFeF₃–SS pristine and that cycled versus Li at different state of charge 189 (D1 V, D2 V, C4.5 V).

Fe K-edge XAS transmission spectra were collected on KFeF₃ 191 samples at different states of charge or discharge at beamline 20-BM-B 192 at the Advanced Photon Source (APS), in transmission mode using a 193 Si (111) double crystal monochromator. A Fe metal standard foil, 194 located in front of a reference ion-chamber for the Fe edge, was 195 measured simultaneously with each spectral sample for energy 196 calibration. All data processing, including normalization, was carried 197 out using the software SIXPACK by fitting a linear polynomial to the 198

199 pre-edge region and a quadratic polynomial to the postedge region of 200 the absorption spectrum. The energy threshold E_0 of the reference Fe 201 foil was determined from the first derivative peak of the spectrum, and 202 all XANES spectra were linearly calibrated using the difference 203 between the obtained E_0 and the tabulated absorption edge energy for 204 Fe K-edge. Pre-edge background subtraction and XANES normal-205 ization were carried out. Background removal and edge-step 206 normalization were performed using Demeter program pack with 207 Athena. IFEFFIT was then used to fit the EXAFS by Artemis in the 208 Demeter software package. 43 The fitting was limited to a k range of 2— 209 10 Å⁻¹, dk = 1 Å⁻¹ using Hanning windows, R range from 1–4 Å. The 210 pristine sample was designated KFeF3-SS pristine, and samples C4.5 211 V, D2 V were KFeF₃-SS cycled versus Li, and Na 1.9 V was cycled 212 versus Na. FeF₂ and FeF₃ are commercial products used as references. Total energy calculations based on density functional theory (DFT) 214 were performed to understand the phase stability of perovskite 215 $\text{Li}_x \text{K}_{1-x} \text{FeF}_3$ and $\text{Na}_x \text{K}_{1-x} \text{FeF}_3$ structures. The relaxed perovskite 216 KFeF₃ structure from the Materials Project was used as the original 217 perovskite framework, whose K sites were replaced with Li (or Na) 218 completely or partially (in supercells) to model distinct K-Li (or K-219 Na) orderings at different compositions.²⁵ The structure enumeration 220 procedure was commonly employed in combination with the cluster 221 expansion formalism to identify low energy structures for a lattice 222 system. 44-46 We calculated 54 structures for Li_xK_{1-x}FeF₃ and 41 223 structures for Na_xK_{1-x}FeF₃. The DFT calculations used the project 224 augmented wave (PAW) method⁴⁷ as implemented in the Vienna ab 225 initio Simulation Package (VASP)⁴⁸ with a plane-wave energy cutoff of 226 520 eV. The generalized gradient approximation (GGA) of Perdew–227 Burke–Ernzerhof (PBE)⁴⁹ was used to approximate the electronic 228 exchange and correlation energy. GGA+U calculations with U 229 parameters consistent with the Materials Project were performed for 230 the fluorides.⁵⁰ The Brillouin-zone integration was sampled with a 231 Monkhorst-Pack mesh of 1000 k-points per atom. Spin polarization was considered with a high spin ferromagnetic initialization. All structures were allowed to fully relax and the total energy was 234 converged within 5 meV per atom. XRD simulations of KFeF₃, 235 $K_{0.5}FeF_3$, and $Li_{0.5}K_{0.5}FeF_3$ were performed with PowderCell 236 software. For the XRD simulations, the same crystal structure and 237 lattice cell parameters were used, and only the site occupancy was 238 changed for three compounds in the simulation to compare the reflection intensity change on varying the A site element.

40 ■ RESULTS AND DISCUSSION

 241 KFeF $_3$ was obtained through a solid state route. The XRD 242 pattern (Figure 1a) matched KFeF $_3$ with a cubic perovskite

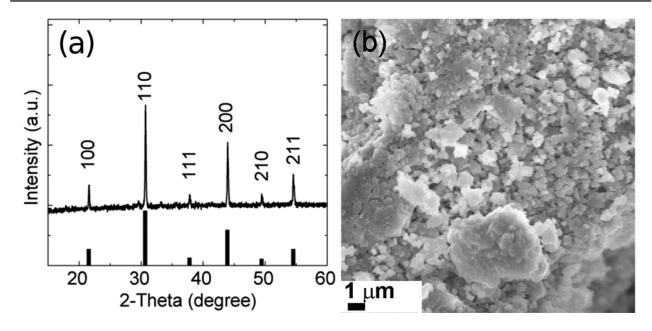


Figure 1. (a) XRD patterns of KFeF₃ compared with reference (PDF#200895), (b) SEM image of KFeF₃.

243 structure (PDF# 200895) showing high crystallinity. One small 244 additional reflection that could not be accounted by KFeF₃ 245 appeared around 30°, 2θ , which was possibly due to a K₂FeF₄ 246 impurity. The intensity indicates that any impurity was present 247 at a very low concentration, and thus, it did not affect the 248 conclusions on KFeF₃ presented hereafter. The morphology 249 and particle size distribution were investigated with SEM

(Figure 1b). The particle size of KFeF₃ was around 1 μ m, as 250 expected from the high temperature calcination routes, with 251 both cubic and spherical particle morphologies (Figure 1b).

To evaluate the ability of KFeF3 to undergo a redox 253 intercalation reaction, the compound was used as the working 254 electrode in a coin cell with an alkali metal (Li or Na) as 255 counter electrode. In the first step, KFeF₃ was driven to anodic 256 (i.e., high) potentials by charging the cell galvanostatically. This 257 step resulted in a relatively steady increase of the cell potentials, 258 which tended to stabilize above 4 V versus Li⁺/Li⁰ and 3.8 V 259 versus Na⁺/Na⁰, respectively. The total accumulated charge 260 after this anodic scan at constant current was roughly 150-170 261 mAh/g, equivalent to the removal of around 80% of K⁺ from 262 the compound. X-ray absorption spectroscopy was measured at 263 the Fe L3-edge for KFeF3 in its pristine state and after the 264 anodic process in the cell against Li metal. Measurements at the 265 Fe L-edge are very sensitive to changes in valence electronic 266 structure since the 2p excitation probes the Fe 3d states, which 267 are directly involved in the redox reactions in batteries. 52 The 268 fluorescence yield (50 nm probing depth) of the Fe L_3 -edge for 269 KFeF₃ at different states of charge is shown in Figure 2b. The 270 f2

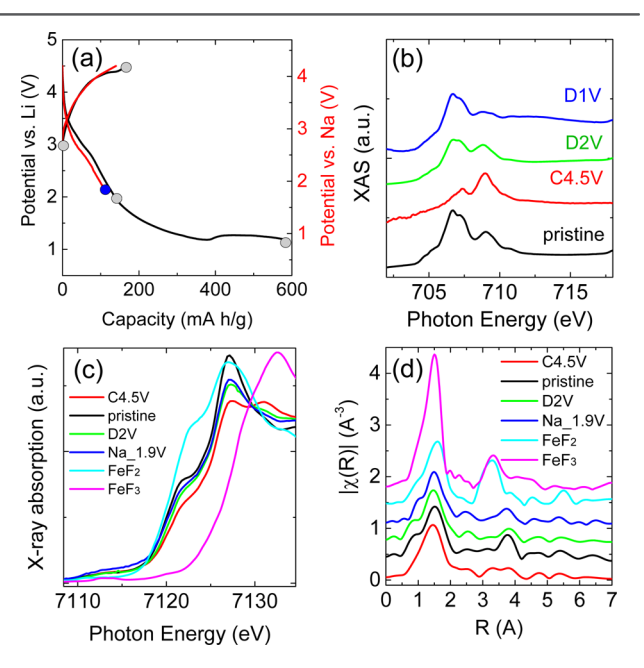


Figure 2. (a) Representative first cycle profile of $A_xK_{1-x}FeF_3$ (A = Li (black), Na (red)). Circles designate samples at different charge/discharge states chosen for XAS study, (b) XAS of Fe *L*-edge of KFeF₃–SS cycled versus Li at different states of charge. (c) XANES (d) and the k^2 extracted EXAFS of the Fe *K*-edge of $A_xK_{1-x}FeF_3$ (A = Li, Na) samples compared with FeF₂ and FeF₃. The solid curves are experimental data, and open circles are fittings.

pristine state showed an intense feature at 706, accompanied by 271 a second one at 709 eV, which is associated with $Fe^{2+.53}$ The 272 intensity ratios of the multiplets are sensitive to changes in the 273 iron oxidation states. The two broad peaks around 706 and 274 709 eV reversed their intensities in the spectrum of when going 275 from the pristine sample compared to the charged state, 276 indicating a transition from Fe^{2+} to Fe^{3+} , with incomplete 277 oxidation. The interference of the tail of the F K-edge (696 278 eV) in the region of the Fe L edge (707 eV) is responsible for a 279 complex background that hindered accurate quantification. 280 Additional information was collected at the Fe K-edge, where 281 changes in oxidation can be clearly observed in the form of 282

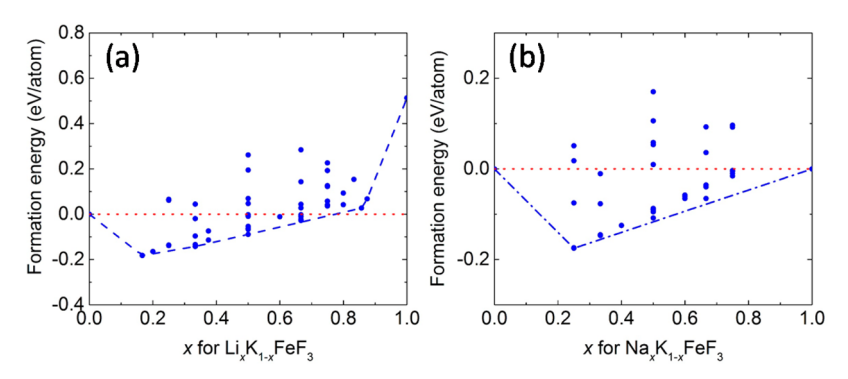


Figure 3. Formation energy of (a) $\text{Li}_x \text{Ki}_{1-x} \text{FeF}_3$ and (b) $\text{Na}_x \text{Ki}_{1-x} \text{FeF}_3$ in a perovskite framework. Each point represents one composition at a particular ordering structure. The relaxed structures with the lowest energy at each calculated composition were connected by dashed lines. The positive formation energies of $\text{Li}_x \text{Ki}_{1-x} \text{FeF}_3$ when x is close to 1 indicate the perovskite framework is unstable at these compositions.

283 solid shifts of the absorption white line, above 7115 eV for 284 KFeF₃ (Figure 2c). A small pre-edge feature can be observed in 285 the spectra of both the materials in the pristine and oxidized state due to the slightly distorted FeF₆ octahedra in the structures. The absorption edge (white line) shifted slightly to higher energy after the anodic scan to 4.5 V versus Li⁺/Li⁰. This state was found to be located between reference spectra of FeF₂ and FeF₃, indicating that mixtures of Fe²⁺/Fe³⁺ were present, as expected from the electrochemistry results and consistent with 292 the L-edge data. Above the absorption edge, the extended X-ray absorption fine structure (EXAFS) region can be analyzed in the form of a radial distribution function through a Fourier transform step. The resulting functions are shown in Figures 2d and S1, with results from fits of the data summarized in Table S1. The similarity in the observed features indicates that the 298 structural changes are small despite the significant change in 299 oxidation state of Fe, as would be expected from a topotactic process of deintercalation of K⁺. The first peak, corresponding 301 to Fe-F bond distances, shifted from 2.05(1) to 2.01(1) Å after 302 the anodic scan on KFeF₃ in a Li metal cell. This observation is 303 consistent with the increase in oxidation state of Fe, which should lead to shorter Fe-F bonds. The values are in line with 305 reported Fe-F bond distances in Fe(III) and Fe(II) fluorides 306 such as FeF₃ (Table S1).^{5,27,55}

After the oxidation step, the polarization of the electro-308 chemical cells was reversed to induce cathodic reactions (cell 309 discharge). The resulting electrochemical profile showed 310 hysteresis with respect to the anodic step (Figure 2a). The 311 potential during the cathodic scan continuously decreased, with 312 the exception of a small inflection point at ~2.8 and 2.5 V 313 versus Li⁺/Li⁰ and Na⁺/Na⁰, respectively. Despite this 314 hysteresis in potential, the specific capacity during charge of 315 the cell was highly reversible upon discharge. While the cell 316 containing Na metal was stopped at 1.9 V versus Na⁺/Na⁰, for a 317 total accumulated capacity of roughly 100 mAh/g, the electrode 318 cycled against Li metal was further reduced to 1.0 V versus Li⁺/ 319 Li^0 . The result was a plateau of potential at $\sim 1.2 \text{ V}$ versus $\text{Li}^+/$ 320 Li⁰, accompanied by a large accumulated specific capacity of 321 almost 600 mAh/g. Fe L3-edge spectra were collected for electrodes stopped at either 2.0 or 1.0 V versus Li⁺/Li⁰ (Figure 2b). The spectrum of the electrode discharged to 2.0 V was consistent with the reduction of Fe³⁺ back to Fe²⁺. Comparison 325 with the pristine state revealed that this reduction was not 326 complete. The center of gravity of the spectrum from a sample 327 collected at 1.0 V was shifted to a lower energy than that of 328 KFeF₃, and the multiplet at higher energy was significantly 329 reduced, which indicated that Fe was reduced beyond the 2+

state. Thus, the process at 1.2 V versus Li⁺/Li⁰ corresponds to 330 the partial conversion to Fe metal, and the destruction of the 331 initial structure, consistent with the very large specific capacity 332 associated with it. Because conversion reactions typically 333 present challenges of reversibility and severe hysteresis, 16,56 334 and due to our fundamental interest in intercalation reactions in 335 these fluorides, further data, discussion, and analysis of this 336 partial conversion to metal are left outside of this study. 337 Comparison of the Fe K-edge spectra at 2.0 V versus Li⁺/Li⁰ 338 with the pristine and oxidized samples revealed a shift back 339 toward Fe²⁺ after the cathodic step (Figure 2c), consistent with 340 the Fe L3-edge data. The Fe K-edge data also indicated that this 341 reduction was not complete. For comparison purposes, the Fe 342 K-edge spectrum of a sample recovered from a Na cell at 1.9 V 343 versus Na⁺/Na⁰ was also collected. The similar signals of the 344 samples harvested at similar potentials prove that Fe can also be 345 reduced in the presence of either Li⁺ and Na⁺. Analysis of the 346 EXAFS data (Figure 2d) revealed a very small change of bond 347 lengths in samples at different Fe oxidation states.

The results presented so far indicate that K+ ions are 349 topotactically removed from KFeF3 to compensate for the 350 partial oxidation of Fe2+ during the cell charge. Since the 351 electrochemical cells are rich in Li⁺ or Na⁺ ions, subsequent 352 reduction must be accompanied by the intercalation of these 353 ions into the perovskite framework to form A,K,FeF₃ (A = Li, 354 Na). Given that these two reactions are different, irrespective of 355 intercalated cation, it is not surprising that hysteresis exists in 356 the electrochemical profile of the anodic and cathodic scan. 357 These results are reminiscent of what was recently reported for 358 KFeSO₄F^{S7} and highlight the chemical flexibility that perovskite 359 structure can accommodate. It also emphasizes the value of 360 electrochemical intercalation reactions as a means to discover 361 new phases; indeed, AxKvFeF3 phases have never been 362 reported. First-principles calculations were performed to 363 investigate their stability. Figure 3 shows the formation energy 364 f3 of perovskite structures with different K-Li and K-Na 365 orderings. The formation energy was defined as in eq 1, 366 where A is Li or Na:

$$\begin{split} E_{\rm F}({\rm K}_{1-x}{\rm A}_x{\rm FeE}_3) &= E({\rm K}_{1-x}{\rm A}_x{\rm FeE}_3) - (1-x)E({\rm KFeE}_3) \\ &- x{\rm E}({\rm AFeE}_3) \end{split} \tag{1)} \ _{368} \end{split}$$

The total energies of perovskite structures for KFeF₃ and 369 NaFeF₃ were used. ²⁵ Because LiFeF₃ is not stable when 370 crystallizing in a perovskite framework, the structure with the 371 lowest predicted energy ($Cmc2_1$, not perovskite structure, 372 where layers of corner- and edge-sharing interconnected [FeF₆] 373



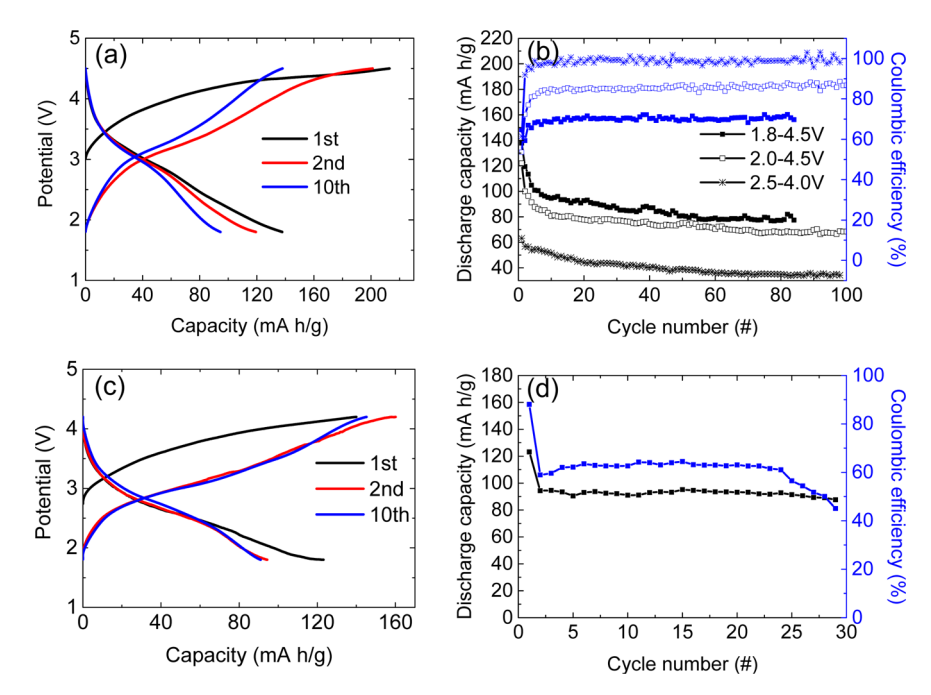


Figure 4. (a) Charge—discharge profiles of a $\text{Li/Li}_x K_{1-x} \text{Fe} F_3$ cell and (b) discharge capacities and Coulombic efficiencies as a function of cycle number using different voltage windows at C/30. (c) Charge—discharge profiles of a Na/Na_xK_{1-x}FeF₃ cell and (d) discharge capacities and Coulombic efficiencies as a function of cycle number between 1.8 and 4.2 V at C/30.

374 octahedra and lithium layers arranged in an alternate fashion in an orthorhombic structure) was taken from the Materials 376 Project (www.materialsproject.org) as a reference. 25 Here, a negative formation energy indicates the binary K-Li (or K-Na) ordering in a perovskite framework is stable against decomposing into two separate phases, KFeF3 and LiFeF3 (or NaFeF₃). As shown in Figure 3, different orderings of K–Li (or K-Na) at certain compositions give different formation energies, and the most stable orderings (lowest formation energies) at selected compositions are shown with a solid curve. The perovskite framework appears to have configurations that are stable for the whole composition range for Na_xK_{1-x}FeF₃ (formation energies lower than 0 eV/atom). However, the perovskite Li_xK_{1-x}FeF₃ phase is only stable up to about 80% Li, due to the energetically unstable cubic perovskite LiFeF3 phase.⁵⁸ In conclusion, density functional theory calculations illustrate that certain perovskite compositions, $A_xK_{1-x}FeF_3$ (A = 391 Li, Na) are thermodynamically stable against decomposition 392 into KFeF3 and LiFeF3 or NaFeF3, which is in agreement with our experimental results. These results also indicate that while full substitution of K+ by Na+ may be possible, leading to very high specific capacity, the substitution of 80% K⁺ by Li⁺, as quantified from the experimental electrochemical data above, may well correspond to the stability limit of the framework.

Once $A_xK_{1-x}FeF_3$ (A = Li, Na) is formed in the working gelectrode, it can be cycled against either Li or Na metal in a highly reversible manner. The specific charge and discharge to apacity curves of the electrochemical cells at selected cycles are shown in Figure 4a and c for Li and Na, respectively. It can be readily observed that the second oxidation occurred with minimal potential hysteresis with respect to the first reduction. This chemical reversibility extended to a significant number of the cycles. The observation indicates that the reaction pathways during charge and discharge are essentially the same after the first cycle so that K^+ ions were removed in the first oxidation, to but either Li⁺ or Na⁺ ions were inserted and extracted

thereafter. Indeed, evidence of both K and Na was found in a 410 carefully rinsed electrode recovered from a Na metal cell after 411 10 cycles based on a combination of SEM and energy dispersive 412 X-ray analysis (Figure S2).

Operando XRD characterization was carried out to further 414 study the structural changes during these electrochemical 415 reactions. Focus was placed on KFeF₃ in a cell with a Li metal 416 counter electrode (and an electrolyte containing a high 417 concentration of Li⁺ ions). The XRD patterns were collected 418 for the first oxidation—reduction cycle as well as a second 419 oxidation. The full patterns are shown in Figure S3, with zooms 420 in the region of the (110) and (200) reflections shown in 421 Figure 5a and b. Two major changes were observed during 422 65

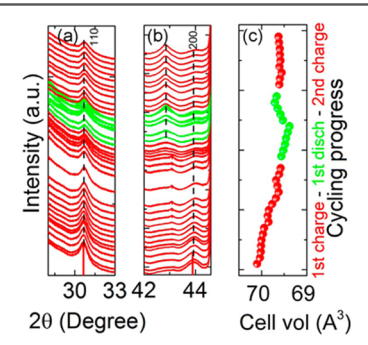


Figure 5. Operando XRD of the 1st cycle and 2nd charge process at the region of (a) (110) and (b) (200), and (c) unit cell volume change calculated from XRD.

cycling: (i) the intensity of the initial KFeF₃ significantly 423 decreased, with no obvious peak shifts; (ii) a new peak 424 appeared during the first discharge. The unit cell volumetric 425 changes of the perovskite lattice upon cycling calculated from 426 XRD patterns are given in Figure 5c. The unit cell volume 427 decreased continuously (within 1% change) during the first 428 charge as K⁺ ions were removed. Relatively little change was 429

430 observed during the subsequent Li $^+$ intercalation/deintercala-431 tion processes, with the exception of an apparent change in 432 trend during the first intercalation, which could be due to a 433 structural relaxation of $\text{Li}_y \text{K}_{1-x} \text{FeF}_3$ (where, ideally, x=y at full 434 reduction), once a critical y was achieved. The overall volume 435 change was less than 1% on cycling. It is worthwhile noting that 436 low values of expansion are favorable in battery electrode 437 materials as this reduces mechanical degradation of the 438 electrode due to the buildup of strain. These results indicate 439 that further exploration of perovskite frameworks in search for 440 viable electrode materials may yield phases with interesting 441 electrochemical properties. The perovskite structure is 442 attractive as it provides 3D channels for ions diffusion, and 443 the original K sites should give more freedom to Li and Na ions 444 to move. 59

This report also provides the first evidence that Fe²⁺ and Li⁺ 445 446 may coexist in a perovskite framework, an interesting 447 observation from the perspective of solid-state chemistry. While it is known that perovskite NaFeF3 has a monoclinic 449 structure due to the distortion introduced by replacing large K⁺ 450 ions (138 pm) with significantly smaller cations, Na⁺ (102 451 pm),⁶⁰ LiFeF₃ has never been successfully synthesized. 452 Interestingly, when stabilized by remaining K⁺ ions, a structure 453 close to the pristine KFeF₃ is retained for the partially lithiated 454 materials. Nonetheless, an intensity decrease was observed in 455 the (110) reflection during the initial K⁺ removal, consistent 456 with it showing the highest density of these cations in the 457 perovskite structure. The subsequent insertion of low-Z Li⁺ 458 ions into the structure is expected to result in a sustained 459 reduced intensity for this reflection. A simple powder XRD 460 simulation of a hypothetical Li_{0.5}K_{0.5}FeF₃ composition con-461 firmed this qualitatively (Figure S4). 51 In the operando 462 experiments, one new reflection appeared to the left of the 463 (200) peak, at around $2\theta = 43^{\circ}$, during the first reduction. The 464 appearance of the new XRD peak is indicative of the lower 465 symmetry of Li_xK_yFeF₃, possibly introduced by ordering of K-466 Li ions or polyhedral distortions known to commonly occur in 467 the perovskite crystal structures. 41,59,61 To evaluate this 468 hypothesis, the XRD patterns of all other relaxed Li_xK_{1-x}FeF₃ 469 structures from DFT calculations were simulated. The 470 simulated XRD patterns reflect the structural changes from 471 the Li replacement of K sites. The new peak in Figure 5b 472 matches the strongest peak of the lowest energy structure of 473 Li_{1/6}K_{5/6}FeF₃ shown in Figure S5. The ordering of Li/K in the 474 structure introduces degeneracy within the perovskite frame-475 work and seems to be stable during early charge/recharge 476 processes of Li_xK_{1-x}FeF₃. The mild inversion of the volume 477 change of Li_xK_vFeF₃ during this first intercalation of Li⁺ noted above would be in line with the ordering of K-Li ions.

Despite the small volume changes during the electrochemical reaction, there was a noticeable capacity loss during the first few the cycles in the Li metal cells (Figure 4b), indicating a few formation cycles are required to reach equilibrium. In contrast, Na metal cells reached a stable cycling performance after the second cycle (Figure 4d); the retention between this cycle and cycle 30 was 95%, compared to 72% for the material in a Li cell. The origin of this different behavior is not clear at this point, although the higher stability of $Na_xK_{1-x}FeF_3$ compared to the Li_xK_{1-x}FeF₃, as reflected in the calculated formation energies in Figure 3, could play a role. The Coulombic efficiencies of the cells was also well below 100% when broad potential windows were used (Figure 4b,d). This behavior indicates that the capacities during oxidation (charge) were systematically higher

than upon reduction (discharge), probably due to the 493 decomposition of electrolyte components at high potential. 494 Nonetheless, the specific capacities stabilized at a respectable 495 ~80 mAh/g and ~90 mAh/g for Li and Na metal cells, 496 respectively, and were sustainable for tens of cycles. As 497 expected, the inefficiencies were reduced when a smaller 498 voltage window was observed, but this came at the expense of 499 lower specific capacities. For instance, when using a window of 500 2.5–4.0 V, the Coulombic efficiency stabilized around 100% 501 with a capacity around 40 mAh/g. Optimization of the 502 electrode performance was beyond the scope of this work 503 and was not attempted.

CONCLUSIONS

In the present study, we have synthesized the parent perovskite 506 KFeF3 through a solid-state chemistry method, and material 507 demonstrated the existence of reversible intercalation chemistry 508 of Li or Na in a K-stabilized Fe-F perovskite framework. XAS 509 at the Fe L3 edge, and XANES and EXAFS at the Fe K-edge 510 probed the $Fe^{2+/3+}$ redox chemistry in $A_xK_{1-x}FeF_3$ (A = Li, Na). 511 Similar local chemical environments and bond lengths of 512 A_xK_{1-x}FeF₃ samples observed at various states of charge 513 collectively substantiate a mechanism of topotactic intercala- 514 tion. In the case of the reaction with Li, operando XRD 515 demonstrated the perovskite structure retention upon inter- 516 calation/extraction, the small volume change being in line with 517 the EXAFS fitting results. DFT calculations suggest that both 518 Li_xK_{1-x}FeF₃ and Na_xK_{1-x}FeF₃ have a relatively broad stable 519 range of compositions crystallizing in the perovskite structure, 520 in agreement with the experimental results. The electro- 521 chemical study on $A_x K_{1-x} Fe F_3$ (A = Li, Na) illustrates this new 522 Fe^{2+/3+} redox chemistry. Moving forward, hypothetically, if 523 phases with high Li contents could be made directly, as 524 opposed to through extraction of K⁺ in an electrochemical cell, 525 even higher specific capacities could be achieved considering 526 the high theoretical capacity of LiFeF₃ (223 mAh/g) and 527 NaFeF₃ (197 mAh/g). Reducing the particle size can help to 528 alleviate the poor conductivity of fluorides, and, consequently, 529 improve the electrochemical performance. These prospects 530 create opportunities for the design of a new family of attractive 531 electrode materials.

ASSOCIATED CONTENT

S Supporting Information

The Supporting Information is available free of charge on the 535 ACS Publications website at DOI: 10.1021/acs.chemma-536 ter.6b04181.

533

534

538

539

540

541

542

543

Additional EXAFS results, SEM, EDX, XRD (PDF)

AUTHOR INFORMATION

Corresponding Author	
*E-mail: jcabana@uic.edu.	
ORCID [®]	
Feng Lin: 0000-0002-3729-3148	

Jordi Cabana: 0000-0002-2353-5986 544

Present Address

Department of Chemistry, Virginia Tech, Blacksburg, Virginia 546 24061, United States. 547

Notes 548 The authors declare no competing financial interest. 549

551 Work at Lawrence Berkeley National Laboratory was supported 552 by the Assistant Secretary for Energy Efficiency and Renewable 553 Energy, Office of Vehicle Technologies of the U.S. Department 554 of Energy (DOE) under Contract No. DE-AC02-05CH11231, 555 as part of the Battery Materials Research (BMR) Program. 556 M.R.P. and J.C. acknowledge research start-up funding by the 557 Department of Chemistry and the College of Liberal Arts and Sciences at the University of Illinois at Chicago. Portions of this 559 research were carried out at the Stanford Synchrotron 560 Radiation Lightsource, a Directorate of SLAC National 561 Accelerator Laboratory and an Office of Science User Facility 562 operated for the U.S. Department of Energy Office of Science 563 by Stanford University. Beamline 20-BM at the Advanced 564 Photon Source (APS) is part of the Pacific Northwest 565 Consortium-X-ray Science Division (PNC/XSD) facilities, 566 supported by the U.S. DOE Office of Science, the Canadian 567 Light Source (CLS), and its funding partners, the University of 568 Washington and the APS. Use of the APS, an Office of Science 569 User Facility operated for the DOE by Argonne National 570 Laboratory, was supported by Contract No. DE-AC02-571 06CH11357.

REFERENCES

- 573 (1) Van Noorden, R. The Rechargable Revolution: A Better Battery. 574 Nature **2014**, 507, 26–28.
- 575 (2) Ma, Y.; Lockwood, G. K.; Garofalini, S. H. Development of a 576 Transferable Variable Charge Potential for the Study of Energy 577 Conversion Materials FeF₂ and FeF₃. *J. Phys. Chem. C* **2011**, *115*, 578 24198–24205.
- 579 (3) Kim, S.-W.; Nam, K.-W.; Seo, D.-H.; Hong, J.; Kim, H.; Gwon, 580 H.; Kang, K. Energy Storage in Composites of a Redox Couple Host 581 and a Lithium Ion Host. *Nano Today* **2012**, *7*, 168–173.
- 582 (4) Tan, H. J.; Smith, H. L.; Kim, L.; Harding, T. K.; Jones, S. C.; 583 Fultz, B. Electrochemical Cycling and Lithium Insertion in Nano-584 structured FeF₃ Cathodes. *J. Electrochem. Soc.* 2014, 161, A445—A449. 585 (5) Li, C.; Yin, C.; Gu, L.; Dinnebier, R. E.; Mu, X.; van Aken, P. A.; 586 Maier, J. An FeF₃·0.5H₂O Polytype: A Microporous Framework 587 Compound with Intersecting Tunnels for Li and Na Batteries. *J. Am.* 588 *Chem. Soc.* 2013, 135, 11425—11428.
- 589 (6) Liu, J.; Wan, Y.; Liu, W.; Ma, Z.; Ji, S.; Wang, J.; Zhou, Y.; 590 Hodgson, P.; Li, Y. Mild and Cost-Effective Synthesis of Iron Fluoride-591 Graphene Nanocomposites for High-Rate Li-ion Battery Cathodes. J. 592 Mater. Chem. A 2013, 1, 1969–1975.
- 593 (7) Li, C.; Gu, L.; Tsukimoto, S.; van Aken, P. A.; Maier, J. Low-594 Temperature Ionic-Liquid-Based Synthesis of Nanostructured Iron-595 Based Fluoride Cathodes for Lithium Batteries. *Adv. Mater.* **2010**, 22, 596 3650–3654.
- 597 (8) Wiaderek, K. M.; Borkiewicz, O. J.; Castillo-Martínez, E.; Robert, 598 R.; Pereira, N.; Amatucci, G. G.; Grey, C. P.; Chupas, P. J.; Chapman, 599 K. W. Comprehensive Insights into the Structural and Chemical 600 Changes in Mixed-Anion FeOF Electrodes by Using Operando PDF 601 and NMR Spectroscopy. *J. Am. Chem. Soc.* 2013, 135, 4070–4078.
- 602 (9) Recham, N.; Rousse, G.; Sougrati, M. T.; Chotard, J.-N.; Frayret, 603 C.; Mariyappan, S.; Melot, B. C.; Jumas, J.-C.; Tarascon, J.-M. 604 Preparation and Characterization of a Stable FeSO₄F-based Frame-605 work for Alkali Ion Insertion Electrodes. *Chem. Mater.* **2012**, *24*, 4363.
- 606 (10) Sobkowiak, A.; Roberts, M.; Häggström, L.; Ericsson, T.; 607 Andersson, A. M.; Edstrom, K.; Gustafsson, T.; Björefors, F. G. 608 Identification of an Intermediate Phase, Li_{1/2}FeSO₄F, Formed During 609 Electrochemical Cycling of Tavorite LiFeSO₄F. *Chem. Mater.* **2014**, 26, 610 4620.
- 611 (11) Badway, F.; Cosandey, F.; Pereira, N.; Amatucci, G. G. Carbon 612 Metal Fluoride Nanocomposites - High-Capacity Reversible Metal 613 Fluoride Conversion Materials as Rechargeable Positive Electrodes for 614 Li Batteries. *J. Electrochem. Soc.* **2003**, *150*, A1318–A1327.

- (12) Kim, S.-W.; Seo, D.-H.; Gwon, H.; Kim, J.; Kang, K. Fabrication $_{615}$ of FeF $_{3}$ Nanoflowers on CNT Branches and Their Application to High $_{616}$ Power Lithium Rechargeable Batteries. *Adv. Mater.* **2010**, 22, 5260–617 5264.
- (13) Amatucci, G. G.; Pereira, N. Fluoride Based Electrode Materials 619 for Advanced Energy Storage Devices. *J. Fluorine Chem.* **2007**, 128, 620 243–262.
- (14) Wang, F.; Robert, R.; Chernova, N. A.; Pereira, N.; Omenya, F.; 622 Badway, F.; Hua, X.; Ruotolo, M.; Zhang, R.; Wu, L.; Volkov, V.; Su, 623 D.; Key, B.; Whittingham, M. S.; Grey, C. P.; Amatucci, G. G.; Zhu, Y.; 624 Graetz, J. Conversion Reaction Mechanisms in Lithium Ion Batteries: 625 Study of the Binary Metal Fluoride Electrodes. *J. Am. Chem. Soc.* 2011, 626 133, 18828–18836.
- (15) Wang, F.; Yu, H.-C.; Chen, M.-H.; Wu, L.; Pereira, N.; 628 Thornton, K.; Van der Ven, A.; Zhu, Y.; Amatucci, G. G.; Graetz, J. 629 Tracking Lithium Transport and Electrochemical Reactions in 630 Nanoparticles. *Nat. Commun.* 2012, 3, 1201.
- (16) Cabana, J.; Monconduit, L.; Larcher, D.; Palacín, M. R. Beyond 632 Intercalation-Based Li-Ion Batteries: The State of the Art and 633 Challenges of Electrode Materials Reacting Through Conversion 634 Reactions. *Adv. Mater.* **2010**, *22*, E170–E192.
- (17) Whittingham, M. S. Ultimate Limits to Intercalation Reactions 636 for Lithium Batteries. *Chem. Rev.* **2014**, *114*, 11414.
- (18) Basa, A.; Gonzalo, E.; Kuhn, A.; Garcia-Alvarado, F. Reaching 638 the Full Capacity of the Electrode Material Li₃FeF₆ by Decreaing the 639 Particle Size to Nanoscale. *J. Power Sources* **2012**, *197*, 260–266.
- (19) Gonzalo, E.; Kuhn, A.; Garcia-Alvarado, F. A Comparative 641 Study of a- and b- Li₃FeF₆: Structure and Electrochemical Behavior. *J.* 642 *Electrochem. Soc.* **2010**, *157*, A1002—A1006.
- (20) Liao, P.; Li, J.; Dahn, J. R. Lithium Intercalation in LiFe₂F₆ and 644 LiMgFeF₆ Disordered Trirutile-Type Phases. *J. Electrochem. Soc.* **2010**, 645 157, A355–A361.
- (21) Lieser, G.; Drager, C.; Schroeder, M.; Indris, S.; de Biasi, L.; 647 Gesswein, H.; Glatthaar, S.; Ehrenberg, H.; Binder, J. R. Sol-Gel Based 648 Synthesis of LiNiFeF₆ and Its Electrochemical Characterzation. *J.* 649 *Electrochem. Soc.* **2014**, *161*, A1071–A1077.
- (22) Shakoor, R. A.; Lim, S. Y.; Kim, H.; Nam, K.-W.; Kang, J. K.; 651 Kang, K.; Choi, J. W. Mechanochemical Synthesis and Electrochemical 652 Behavior of Na₃FeF₆ in Sodium and Lithium Batteries. *Solid State* 653 *Ionics* 2012, 218, 35–40.
- (23) Tressaud, A.; Portier, J.; de Pape, R.; Hagenmuller, P. Les 655 Systèmes MF-FeF₃ (M = Li, Na, K, Rb, Cs, Tl, NH₄). J. Solid State 656 Chem. 1970, 2, 269–277.
- (24) Tressaud, A.; Portier, J.; Shearer-Turrell, S.; Dupin, J.-L.; 658 Hagenmuller, P. Les Hexafluoferrites M_3 FeF $_6$ (M= Li, Na, K, Rb, Cs, 659 Ag, Tl, NH $_4$): Etude Radiocristallographique, Spectroscopique et 660 Magnetique. J. Inorg. Nucl. Chem. 1970, 32, 2179–2186.
- (25) Jain, A.; Ong, S. P.; Hautier, G.; Chen, W.; Richards, W. D.; 662 Dacek, S.; Cholia, S.; Gunter, D.; Skinner, D.; Ceder, G.; Persson, K. 663 A. Commentary: The Materials Project: A Materials Genome 664 Approach to Accelerating Materials Innovation. *APL Mater.* **2013**, *1*, 665 011002.
- (26) Rudowicz, C.; Piwowarska, D. Spectroscopic Properties of Fe²⁺ 667 Ions at Tetragonal Sites-Crystal Field Effects and Microscopic 668 Modeling of Spin Hamiltonian Parameters for Fe²⁺ (S=2) Ions in 669 K_2 FeF₄ and K_2 ZnF₄. J. Magn. Magn. Mater. **2011**, 323, 2681–2689. (27) Okazaki, A.; Suemune, Y. The Crystal Structures of KMnF₃, 671
- (27) Okazaki, A.; Suemune, Y. The Crystal Structures of KMnF₃, 671 KFeF₃, KCoF₃, KNiF₃ and KCuF₃ Above and Below Their Neel 672 Temperatures. *J. Phys. Soc. Jpn.* **1961**, *16*, 671–675.
- (28) Yamada, Y.; Doi, T.; Tanaka, I.; Okada, S.; Yamaki, J.-i. Liquid- 674 phase Synthesis of Highly Dispersed NaFeF₃ Particles and Their 675 Electrochemical Properties for Sodium-ion Batteries. *J. Power Sources* 676 **2011**, 196, 4837–4841.
- (29) Pena, M. A.; Fierro, J. L. G. Chemical Structures and 678 Performance of Perovskite Oxides. *Chem. Rev.* **2001**, *101*, 1981–2017. 679 (30) Goldschmidt, V. V. M Die Gesetze der Krystallochemie. 680 *Naturwissenschaften* **1926**, *14* (21), 477.
- (31) Dimov, N.; Nishimura, A.; Chihara, K.; Kitajou, A.; Gocheva, I. 682 D.; Okada, S. Transition Metal NaMF₃ Compounds as Model Systems 683

- 684 for Studying the Feasibility of Ternary Li-M-F and Na-M-F Single 685 Phases as Cathodes for Lithium—ion and Sodium—ion Batteries. 686 Electrochim. Acta 2013, 110, 214—220.
- 687 (32) Ishihara, T.; Matsuda, H.; Takita, Y. Doped LaGaO₃ Perovskite 688 Type Oxide as a New Oxide Ionic Conductor. *J. Am. Chem. Soc.* **1994**, 689 *116*, 3801–3803.
- 690 (33) Thangadurai, V.; Shukla, A. K.; Gopalakrishnan, J. 691 La_{0.9}Sr_{0.1}Ga_{0.8}Mn_{0.2}O_{2.85}: a New Oxide Ion Conductor. *Chem.* 692 *Commun.* **1998**, 2647–2648.
- 693 (34) Feng, M.; Goodenough, J. B. A Superior Oxide-ion Electrolyte. 694 Eur. J. Solid State Inorg. Chem. 1994, 31, 663–672.
- 695 (35) Steele, B. C. H.; Bae, J.-M. Properties of La_{0.6}Sr_{0.4}Co_{0.2}Fe_{0.8}O_{3-x} 696 (LSCF) Double Layer Cathodes on Gadolinium-doped Cerium Oxide 697 (CGO) Electrolytes: II. Role of Oxygen Exchange and Diffusion. *Solid* 698 State Ionics **1998**, 106, 255–261.
- 699 (36) Green, M. A.; Ho-Baillie, A.; Snaith, H. J. The Emergence of 700 Perovskite Solar Cells. *Nat. Photonics* **2014**, *8*, 506–514.
- 701 (37) Sullivan, E.; Avdeev, M.; Vogt, T. Structural Distortions in 702 $Sr_{3-x}A_xMO_4F$ (A=Ca, Ba; M=Al, Ga, In) Anti-Perovskites and 703 Corresponding Changes in Photoluminescence. *J. Solid State Chem.* 704 **2012**, 194, 297–306.
- 705 (38) Suntivich, J.; May, K. J.; Gasteiger, H. A.; Goodenough, J. B.; 706 Shao-Horn, Y. A Perovskite Oxide Optimized for Oxygen Evolution 707 Catalysis from Molecular Orbital Principles. *Science* **2011**, 334, 1383–708 1385.
- 709 (39) Han, X.; Hu, Y.; Yang, J.; Cheng, F.; Chen, J. Porous Perovskite 710 CaMnO₃ as an Electrocatalyst for Rechargeable Li-O2 Batteries. *Chem.* 711 *Commun.* **2014**, *50*, 1497—1499.
- 712 (40) Takada, K. Secondary Batteries—Lithium Rechargable Systems—713 Lithium-ion Electrolytes: Solid Oxide. In *Encyclopedia of Electro-*714 *chemical Power Sources*; Garche, J., Ed.; Elsevier: Amsterdam, 2009; pp 715 328—336.
- 716 (41) Wang, G. X.; Yao, P.; Bradhurst, D. H.; Dou, S. X.; Liu, H. K. 717 Structure Characterisation and Lithium Insertion in La_{0.33}NbO₃ 718 Perovskite. *Solid State Ionics* **1999**, *124*, 37–43.
- 719 (42) Doeff, M. M.; Chen, G.; Cabana, J.; Richardson, T. J.; Mehta, A.; 720 Shirpour, M.; Duncan, H.; Kim, C.; Kam, K. C.; Conry, T. 721 Characterization of Electrode Materials for Lithium Ion and Sodium 722 Ion Batteries Using Synchrotron Radiation Techniques. *J. Visualized* 723 Exp. 2013, e50594.
- 724 (43) Ravel, B.; Newville, M. ATHENA; ARTEMIS; HEPHAESTUS, 725 Data Analysis for X-ray Absorption Sepctroscopy Using IFEFFIT. J. 726 Synchrotron Radiat. 2005, 12, 537–541.
- 727 (44) van de Walle, A.; Ceder, G. Automating First-principles Phase 728 Diagram Calculations. *J. Phase Equilib.* **2002**, 23, 348–359.
- 729 (45) Chen, W.; Dalach, P.; Schneider, W. F.; Wolverton, C. Interplay 730 Between Subsurface Ordering, Surface Segregation, and Adsorption on 731 Pt—Ti(111) Near-Surface Alloys. *Langmuir* **2012**, *28*, 4683—4693.
- 732 (46) Chen, W.; Schmidt, D.; Schneider, W. F.; Wolverton, C. First-733 principles Cluster Expansion Study of Missing-row Reconstructions of 734 FCC (110) Surfaces. *Phys. Rev. B: Condens. Matter Mater. Phys.* **2011**, 735 83, 075415.
- 736 (47) Kresse, G.; Joubert, D. From Uultrasoft Pseudopotentials to the 737 Projector Augmented-wave Method. *Phys. Rev. B: Condens. Matter* 738 *Mater. Phys.* 1999, 59, 1758–1775.
- 739 (48) Kresse, G.; Furthmüller, J. Efficient Iterative Schemes for Ab 740 initio Total-energy Calculations Using a Plane-wave Basis Set. Phys. 741 Rev. B: Condens. Matter Mater. Phys. 1996, 54, 11169–11186.
- 742 (49) Perdew, J. P.; Burke, K.; Ernzerhof, M. Generalized Gradient 743 Approximation Made Simple. *Phys. Rev. Lett.* **1996**, *77*, 3865–3868.
- 744 (50) Jain, A.; Hautier, G.; Moore, C. J.; Ping Ong, S.; Fischer, C. C.; 745 Mueller, T.; Persson, K. A.; Ceder, G. A high-throughput infrastructure 746 for density functional theory calculations. *Comput. Mater. Sci.* **2011**, 50, 2275 2320
- 748 (51) Kraus, W.; Nolze, G. *PowderCell*, 2.4; Federal Institute for 749 Materials Research and Testing: Berlin, Germany, 2000.
- 750 (52) Giorgetti, M. A Review on the Structural Studies of Batteries 751 and Host Materials by X-Ray Absorption Spectroscopy. *ISRN Mater.* 752 *Sci.* **2013**, 2013, 938625.

- (53) Liu, X.; Liu, J.; Qiao, R.; Yu, Y.; Li, H.; Suo, L.; Hu, Y.-S.; 753 Chuang, Y.-D.; Shu, G.; Chou, F.; Weng, T.-C.; Nordlund, D.; Sokaras, 754 D.; Wang, Y. J.; Lin, H.; Barbiellini, B.; Bansil, A.; Song, X.; Liu, Z.; 755 Yan, S.; Liu, G.; Qiao, S.; Richardson, T. J.; Prendergast, D.; Hussain, 756 Z.; de Groot, F. M. F.; Yang, W. Phase Transformation and Lithiation 757 Effect on Electronic Structure of Li_xFePO₄: An In-Depth Study by Soft 758 X-ray and Simulations. J. Am. Chem. Soc. 2012, 134, 13708–13715. 759 (54) Graetz, J.; Ahn, C. C.; Ouyang, H.; Rez, P.; Fultz, B. White 760 Lines and d-band Occupancy for the 3d Transition-metal Oxides and 761 Lithium Transition-metal Oxides. Phys. Rev. B: Condens. Matter Mater. 762 Phys. 2004, 69, 235103.
- (55) Knox, K. Perovskite-Like Fluorides: I. Structures of KMnF₃, 764 KFeF₃, KCoF₃, KNiF₃ and KZnF₃. Crystal Field Effects in the Series 765 and in KCrF₃ and KCuF₃. Acta Crystallogr. **1961**, 14, 583.
- (56) Ko, J. K.; Wiaderek, K. M.; Pereira, N.; Kinnibrugh, T. L.; Kim, 767 J. R.; Chupas, P. J.; Chapman, K. W.; Amatucci, G. G. Transport, 768 Phase Reactions, and Hysteresis of Iron Fluoride and Oxyfluoride 769 Conversion Electrode Materials for Lithium Batteries. ACS Appl. 770 Mater. Interfaces 2014, 6, 10858–10869.
- (57) Yang, F.; Liu, Y.; Martha, S. K.; Wu, Z.; Andrews, J. C.; Ice, G. 772 E.; Pianetta, P.; Nanda, J. Nanoscale Morphological and Chemical 773 Changes of High Voltage Lithium—Manganese Rich NMC Composite 774 Cathodes with Cycling. *Nano Lett.* **2014**, *14*, 4334–4341.
- (58) Doe, R. E.; Persson, K. A.; Meng, Y. S.; Ceder, G. First- 776 Principles Investigation of the Li-Fe-F Phase Diagram and 777 Equilibrium and Nonequilibrium Conversion Reactions of Iron 778 Fluorides with Lithium. *Chem. Mater.* **2008**, 20, 5274–5283.
- (59) Inoue, N.; Zou, Y. Physical Properties of Perovskite-type 780 Lithium Ionic Conductor. *Physics of Solid State Ionics* **2006**, 247–269. 781
- (60) Shannon, R. Revised Effective Ionic Radii and Systematic 782 Studies of Interatomic Distances in Halides and Chalcogenides. *Acta* 783 *Crystallogr., Sect. A: Cryst. Phys., Diffr., Theor. Gen. Crystallogr.* **1976**, 32, 784 751–767.
- (61) Gabrisch, H.; Yi, T.; Yazami, R. Transmission Electron 786 Microscope Studies of $\text{LiNi}_{1/3}\text{Mn}_{1/3}\text{Co}_{1/3}\text{O}_2$ before and after Long- 787 Term Aging at 70 °C. *Electrochem. Solid-State Lett.* **2008**, *11*, A119 788 A124.
- (62) Lux, S. F.; Pollak, E.; Boesenberg, U.; Richardson, T.; Kostecki, 790 R. Electrochemical Reactivity of Pyrolytic Carbon Film Electrodes in 791 Organic Carbonate Electrolytes. *Electrochem. Commun.* **2014**, *46*, 5–8. 792